Short Article

Structure

Slow conformational dynamics of the human A_{2A} adenosine receptor are temporally ordered

Graphical abstract

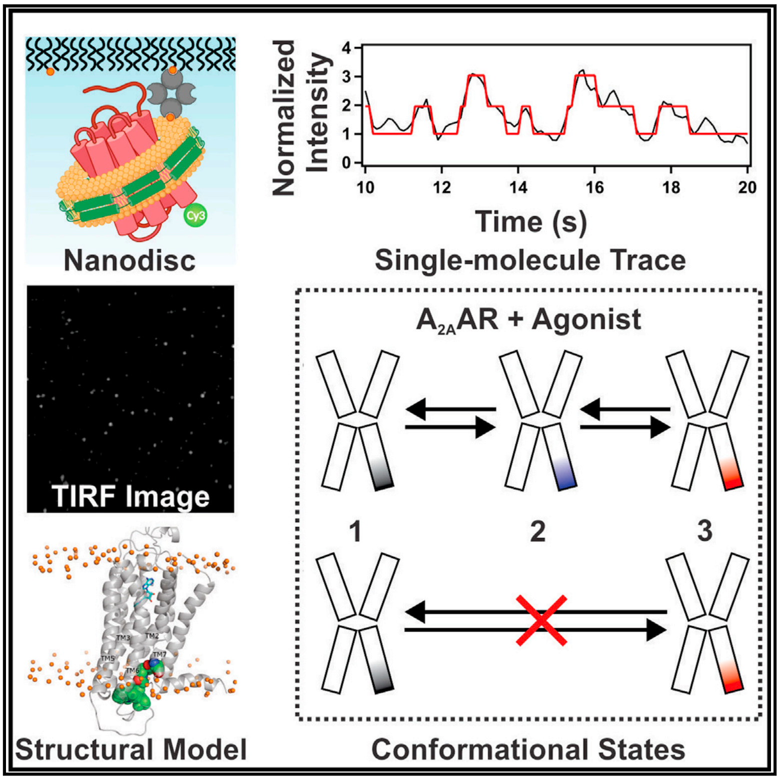

Highlights

- Single-molecule fluorescence observes slow dynamic behavior of A_{2A}AR complexes
- Three different fluorescence emission states observed for A_{2A}AR complexes with agonists
- Reversible transitions among different states occurred in a sequential order
- A functionally critical transition state not represented among available structures

Authors

Shushu Wei, Naveen Thakur,
Arka P. Ray, ...,
Hugo Gutiérrez-de-Terán,
Matthew T. Eddy, Rajan Lamichhane

Correspondence

rajan@utk.edu (R.L.),
matthew.eddy@chem.ufl.edu (M.T.E.)

In brief

Wei et al. use single-molecule fluorescence to observe slow exchange among at least three conformations of the agonist-bound A_{2A} adenosine receptor. Transitions from inactive to active-like conformations are sequential and must proceed through an intermediate state not currently represented among available structures.

Wei et al., 2022, Structure *30*, 329–337
March 3, 2022 © 2021 Elsevier Ltd.
https://doi.org/10.1016/j.str.2021.11.005

CellPress

Structure

CellPress

Short Article

Slow conformational dynamics of the human A_{2A} adenosine receptor are temporally ordered

Shushu Wei,[1] Naveen Thakur,[2] Arka P. Ray,[2] Beining Jin,[2] Samuel Obeng,[3,4] Christopher R. McCurdy,[4,5] Lance R. McMahon,[3] Hugo Gutiérrez-de-Terán,[6] Matthew T. Eddy,[2,*] and Rajan Lamichhane[1,7,*]
[1]Department of Biochemistry & Cellular and Molecular Biology, College of Arts and Sciences, University of Tennessee, 1311 Cumberland Avenue, Knoxville, TN 37932, USA
[2]Department of Chemistry, College of Liberal Arts and Sciences, University of Florida, 126 Sisler Hall, Gainesville, FL 32611, USA
[3]Department of Pharmacodynamics, College of Pharmacy, University of Florida, Gainesville, FL 32610, USA
[4]Department of Medicinal Chemistry, College of Pharmacy, University of Florida, Gainesville, FL 32610, USA
[5]Translational Drug Development Core, Clinical and Translational Sciences Institute, University of Florida, Gainesville, FL 32610, USA
[6]Department of Cell and Molecular Biology, Uppsala University, B.M.C., Box 596, Uppsala 751 24, Sweden
[7]Lead contact
*Correspondence: rajan@utk.edu (R.L.), matthew.eddy@chem.ufl.edu (M.T.E.)
https://doi.org/10.1016/j.str.2021.11.005

SUMMARY

A more complete depiction of protein energy landscapes includes the identification of different function-related conformational states and the determination of the pathways connecting them. We used total internal reflection fluorescence (TIRF) imaging to investigate the conformational dynamics of the human A_{2A} adenosine receptor (A_{2A}AR), a class A G protein-coupled receptor (GPCR), at the single-molecule level. Slow, reversible conformational exchange was observed among three different fluorescence emission states populated for agonist-bound A_{2A}AR. Transitions among these states predominantly occurred in a specific order, and exchange between inactive and active-like conformations proceeded through an intermediate state. Models derived from molecular dynamics simulations with available A_{2A}AR structures rationalized the relative fluorescence emission intensities for the highest and lowest emission states but not the transition state. This suggests that the functionally critical intermediate state required to achieve activation is not currently visualized among available A_{2A}AR structures.

INTRODUCTION

Time-dependent fluctuations of the atomic coordinates of proteins, i.e., conformational dynamics, are inherently related to their biological functions, as demonstrated over 40 years ago by nuclear magnetic resonance (NMR) spectroscopy (Wagner et al., 1976; Wüthrich and Wagner, 1975) and subsequent additional biophysical methods. An understanding of protein conformational dynamics is necessary to develop fundamental mechanistic insights into processes such as protein-substrate and protein-protein interactions in biological systems.

These same molecular recognition processes give rise to the physiological activities of G protein-coupled receptors (GPCRs), sensory proteins that bind an enormous range of endogenous and exogenous ligands, including many hormones, neurotransmitters, and clinical drugs (Hauser et al., 2017). Chemical information contained in bound ligands is relayed to the GPCR intracellular surface through conformational dynamics that enable receptors to recognize intracellular partner proteins and initiate signaling cascades. Information on function-related dynamics has predominantly been provided by spectroscopic methods, which complement GPCR structures from X-ray crystallography and cryogenic electron microscopy (cryo-EM) (Bostock et al., 2019; Shimada et al., 2019). Many spectroscopic methods, including NMR spectroscopy, typically observe average properties of proteins from a large ensemble of molecules. These spectroscopic methods can identify multiple, simultaneously populated conformational states. However, when more than two states are observed, information on the pathways connecting different states and, importantly, the order in which they are populated must come from single-molecule measurements (Aviram et al., 2018; Chung et al., 2012; Kim and Chung, 2020; Schuler et al., 2002).

We used single-molecule fluorescence to study the conformational dynamics of the human A_{2A} adenosine receptor (A_{2A}AR), a representative class A GPCR. A_{2A}AR has been the focus of a growing number of NMR spectroscopic studies (Clark et al., 2017; Eddy et al., 2017, 2018, 2021; Huang et al., 2021; Mizumura et al., 2020; Sušac et al., 2018; Ye et al., 2016, 2018), which provide a rich set of literature data as a background for the further development of additional biophysical methods to study GPCRs. Thus, it seemed to be a logical next step to extend single-molecule fluorescence experiments developed to study the β_2-adrenergic receptor (Gregorio et al., 2017; Lamichhane et al., 2015, 2020) to $A_{2A}AR$ as a second member of class A GPCRs.

Using single-molecule total internal reflection fluorescence (TIRF) imaging, we observed relatively slower ($k_{ex} \leq 10\ s^{-1}$) exchange processes in $A_{2A}AR$ with a fluorophore covalently attached to helix 7 at the intracellular surface. Our data complement other $A_{2A}AR$ studies that investigated relatively faster timescales using single-molecule Förster resonance energy transfer (FRET), which measured ligand efficacy-dependent changes for sub-millisecond to ~3 millisecond molecular motions of $A_{2A}AR$ in detergent micelles (Fernandes et al., 2021) and in lipid nanodiscs (Maslov et al., 2020). In the present study, measurements of slower exchange processes provide an exciting window into $A_{2A}AR$ function-related conformational dynamics.

RESULTS

$A_{2A}AR$ sample preparation and TIRF imaging experimental design

For single-molecule fluorescence imaging experiments, a variant of human $A_{2A}AR$ containing a single cysteine replacement at position 289 located at the intracellular surface of helix 7, $A_{2A}AR$ [A289C], was expressed in *Pichia pastoris* using previously described protocols (see STAR Methods) (Eddy et al., 2017). The location of the introduced cysteine was selected based on literature data from ^{19}F NMR studies of $A_{2A}AR$ (Sušac et al., 2018), which demonstrated that NMR spectra of $A_{2A}AR$ labeled with ^{19}F-2,2,2-trifluoroethanethiol at the same position were sensitive to differences in the efficacies of bound ligands (Sušac et al., 2018). C289 was the only cysteine available for chemical conjugation. Purified $A_{2A}AR$[A289C] was reconstituted into lipid nanodiscs containing a 65:30:5 molar ratio mixture of 1-palmitoyl-2-oleoyl-glycero-3-phosphocholine (POPC), 1-palmitoyl-2-oleoyl-sn-glycero-3-phospho-L-serine (POPS), and biotinylated 1-palmitoyl-2-oleoyl-glycero-3-phosphoethanolamine (POPE) lipids, respectively, and labeled with the Cy3 fluorophore at position 289, yielding homogeneous sample preparations (Figure S1). $A_{2A}AR$[A289C] labeled with Cy3 in lipid nanodiscs retained nearly native ligand binding affinities for antagonists and agonists, as measured by radioligand binding experiments on the same samples measured in single-molecule fluorescence experiments (Figure S1). In the following sections, Cy3-labeled $A_{2A}AR$[A289C] is referred to as $A_{2A}AR$-Cy3.

To investigate the conformational dynamics of $A_{2A}AR$ at the single-molecule level, we immobilized nanodiscs containing $A_{2A}AR$-Cy3 on a microscope slide and monitored them under TIRF illumination, following protocols established in single-molecule fluorescence experiments with the β_2-adrenergic receptor (Lamichhane et al., 2015, 2020). The resolution of the camera used in TIRF imaging experiments enabled observations of changes in fluorescence emission on the timescale of ≥ 100 milliseconds, correlating to rates of exchange processes of $k_{ex} \leq 10\ s^{-1}$. Control experiments were performed to characterize the specific immobilization of biotin-labeled nanodiscs to a PEG-coated quartz slide surface using biotin-streptavidin interactions (Figure S2). Fluorescence time trajectories were measured for $A_{2A}AR$-Cy3 with no ligand added during the sample preparation, i.e., apo $A_{2A}AR$-Cy3 (Figure 1A), and for $A_{2A}AR$-Cy3 in complexes with the antagonist ZM241385 and agonists NECA (Figure 1B) and CGS21680. Following protocols validated in earlier TIRF studies with GPCRs (Lamichhane et al., 2015, 2020), subsequent analysis focused on data from dynamic molecules from folded and functional receptors. Approximately 40%–50% of the trajectories showed dynamic behavior, comparable to earlier studies with β_2AR in lipid nanodiscs, where approximately 60% of the molecules showed dynamic behavior (Leitz et al., 2006; Rouck et al., 2017).

Two predominant fluorescence emission states are observed with apo and antagonist-bound $A_{2A}AR$ in lipid nanodiscs

The majority of apo $A_{2A}AR$-Cy3 trajectories showed dynamic behavior where the fluorescence intensity reversibly fluctuated primarily between two intensity states (Figures 1A and S3). We normalized the fluorescence intensities with the mean intensity of the lowest intensity state at each point and compiled traces of 239 individual molecules to generate a histogram (Figure 1C). The histogram shows two distinct peaks centered around two different intensity states with relative areas of 62% and 38% that we assigned as state 1 and state 2, respectively (Figure 1C).

Similar to apo $A_{2A}AR$-Cy3, the majority of $A_{2A}AR$-Cy3 molecules in complex with the antagonist ZM241385 also showed dynamic behavior with fluorescence intensities that fluctuated between two intensity states (Figure 1E), with the same mean fluorescence emission intensities observed for apo $A_{2A}AR$-Cy3. The resulting histogram generated from single-molecule traces of 288 molecules of $A_{2A}AR$-Cy3 in complex with ZM241385 showed two distinct states centered around the same intensity values as apo $A_{2A}AR$-Cy3 with relative areas of 59% for state 1 and 41% for state 2, comparable to observations with apo $A_{2A}AR$-Cy3 (Figures 1C and 1E). For both apo and antagonist-bound $A_{2A}AR$-Cy3, we also observed a relatively small population of transitions to an even higher third intensity state (Figures 2D and 2F); however, the number of these transitions was not sufficient to populate this state on the histogram.

Three fluorescence emission states are observed with agonist-bound $A_{2A}AR$ in lipid nanodiscs

Single-molecule fluorescence traces of $A_{2A}AR$-Cy3 in complexes with the agonists NECA and CGS21680 showed dynamic behavior for a majority of the observed molecules. In traces of agonist-bound $A_{2A}AR$-Cy3, three distinct emissions intensities were observed (Figure 1B). For the $A_{2A}AR$-Cy3 complex with NECA, traces from 229 molecules were compiled into a histogram (Figure 1D), which showed distinct changes compared with the histograms for apo and antagonist-bound $A_{2A}AR$-Cy3. Compared to apo and antagonist-bound $A_{2A}AR$-Cy3, the histogram for $A_{2A}AR$-Cy3 in complex with NECA showed a decrease in the population of state 1 (49%), similar population of state 2 (39%), and the emergence of a third population, which we defined as state 3 (12%) (Figure 1D). Single-molecule experiments with $A_{2A}AR$-Cy3 in complex with a second agonist, CGS21680, showed similar behavior to the complex with NECA. A histogram compiled from traces of 315 molecules of $A_{2A}AR$-Cy3 in complex with CGS21680 showed three distinct states with relative areas of 46%, 39%, and 15% calculated for States 1, 2, and 3, respectively (Figure 1F).

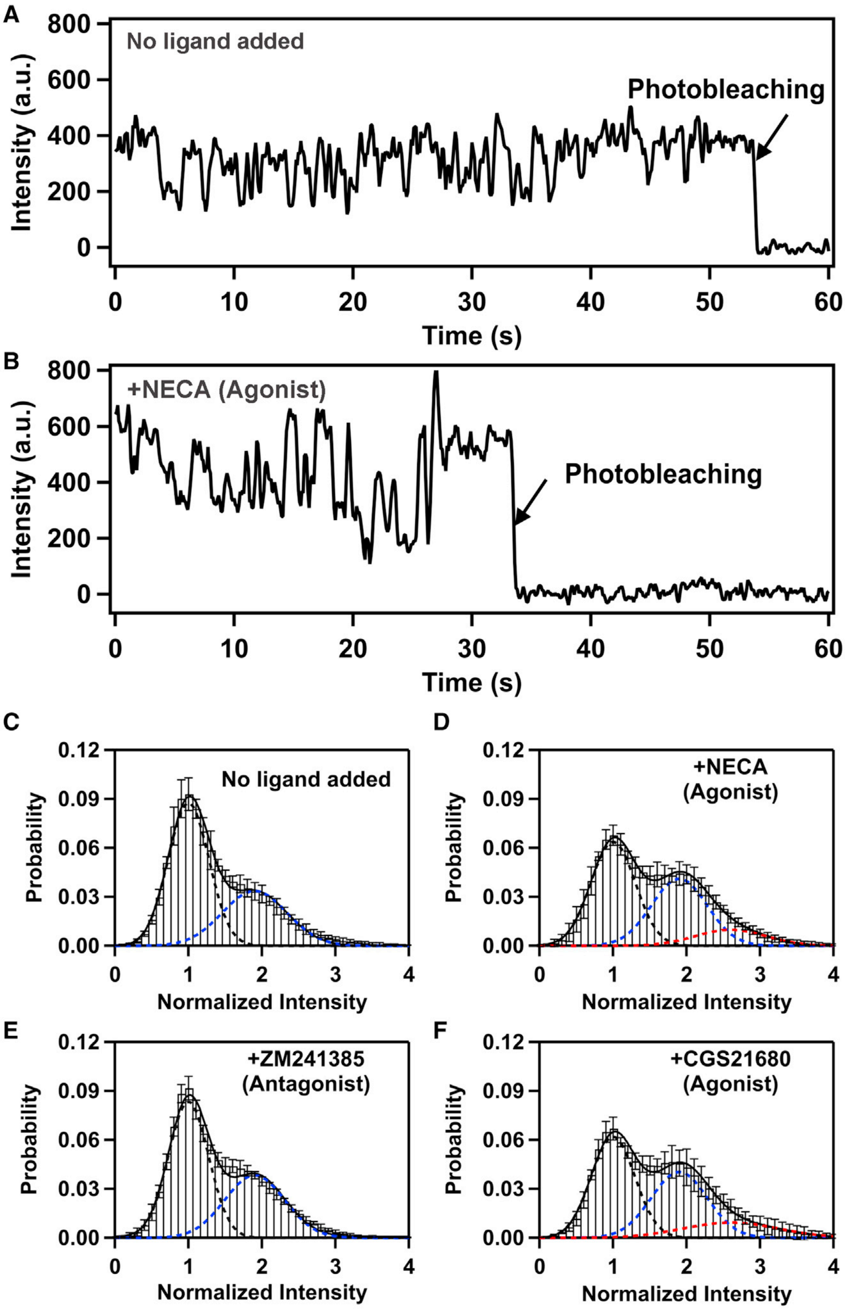

Figure 1. Single-molecule fluorescence intensity trajectories and histograms compiled from a collection of individual A_{2A}AR molecules

(A) An example single-molecule fluorescence intensity trajectory from immobilized apo A_{2A}AR-Cy3 in lipid nanodiscs. Repeated intensity jumps are observed predominantly between two fluorescence intensity states at ~200 and ~400 a.u. before photobleaching. The trajectory shows raw intensities without normalization or fitting with a hidden Markov model. Loss of intensity fluctuations after a single-step photobleaching transition (black arrow) indicates a single receptor molecule is observed.

(B) Single-molecule fluorescence intensity trajectory of A_{2A}AR in complex with the agonist NECA. Intensity jumps are observed among three intensity states at ~200, ~400, and ~600 a.u. Same presentation details as in (A). The selected trace shows the range of transitions between different events, including several transitions to state 3 before photobleaching.

(C) Histogram compiled from 239 receptor molecules of A_{2A}AR, where no ligand was added to the sample (apo). The dashed black and blue lines represent fits to two Gaussian populations centered around the normalized intensities of 1 and 2. Fluorescence intensities are normalized to the mean intensity of the low-intensity state. The composite fit representing the sum of the two Gaussian fitted curves is shown as the solid black line. Error bars represent the standard error calculated for each bar of the histogram.

(D) Histogram compiled from 229 receptor molecules of A_{2A}AR in complex with the agonist NECA. The dotted black and blue lines represent fits to two Gaussian populations centered around the normalized intensities of 1 and 1.9 , and the red dotted curve represents a fit to a third Gaussian population centered around the normalized intensity of 2.6 . The composite fit representing the sum of the three Gaussian fitted curves is shown as the solid black line. Other presentation details same as in (C).

(E) Histogram compiled from 288 receptor molecules of A_{2A}AR in complex with the antagonist ZM241385. Same presentation details as in (C).

(F) Histogram compiled from 315 receptor molecules of A_{2A}AR in complex with the agonist CGS21680. Same presentation details as in (D).

See also Figures S1 and S2.

Structural models of A_{2A}AR-Cy3 provide a rational for two of the observed fluorescence intensities

Because the Cy3 fluorescence emission intensity depends on the local environment of the fluorophore, changes in the fluorescence emission are strongly correlated with changes in protein structure and the environment of Cy3 (Hwang et al., 2011; Lamichhane et al., 2015, 2020; Stennett et al., 2015). To investigate the structural basis for the observed different fluorescence intensities of A_{2A}AR-Cy3 complexes, we generated three computational models of A_{2A}AR-Cy3 by covalently docking the fluorophore to representative crystal structures of human A_{2A}AR and followed this with extensive atomistic molecular dynamics (MD) simulations (see STAR Methods). From these models, we investigated the range of possible orientations of Cy3 and the local environment around the dye, which can control the conformational degrees of freedom of the dye and influence fluorescence emission intensities.

Three structures were chosen as representatives for generating the initial models: A_{2A}AR in complex with the antagonist ZM241385 (PDB ID 4EIY) (Liu et al., 2012), A_{2A}AR in complex with the full agonist NECA (PDB ID 2YDV) (Lebon et al., 2011), and a tertiary complex with NECA and an engineered G protein, “mini $G\alpha_S$” (PDB ID 5G53) (Carpenter et al., 2016). For each case, the initial model was created by manually covalently

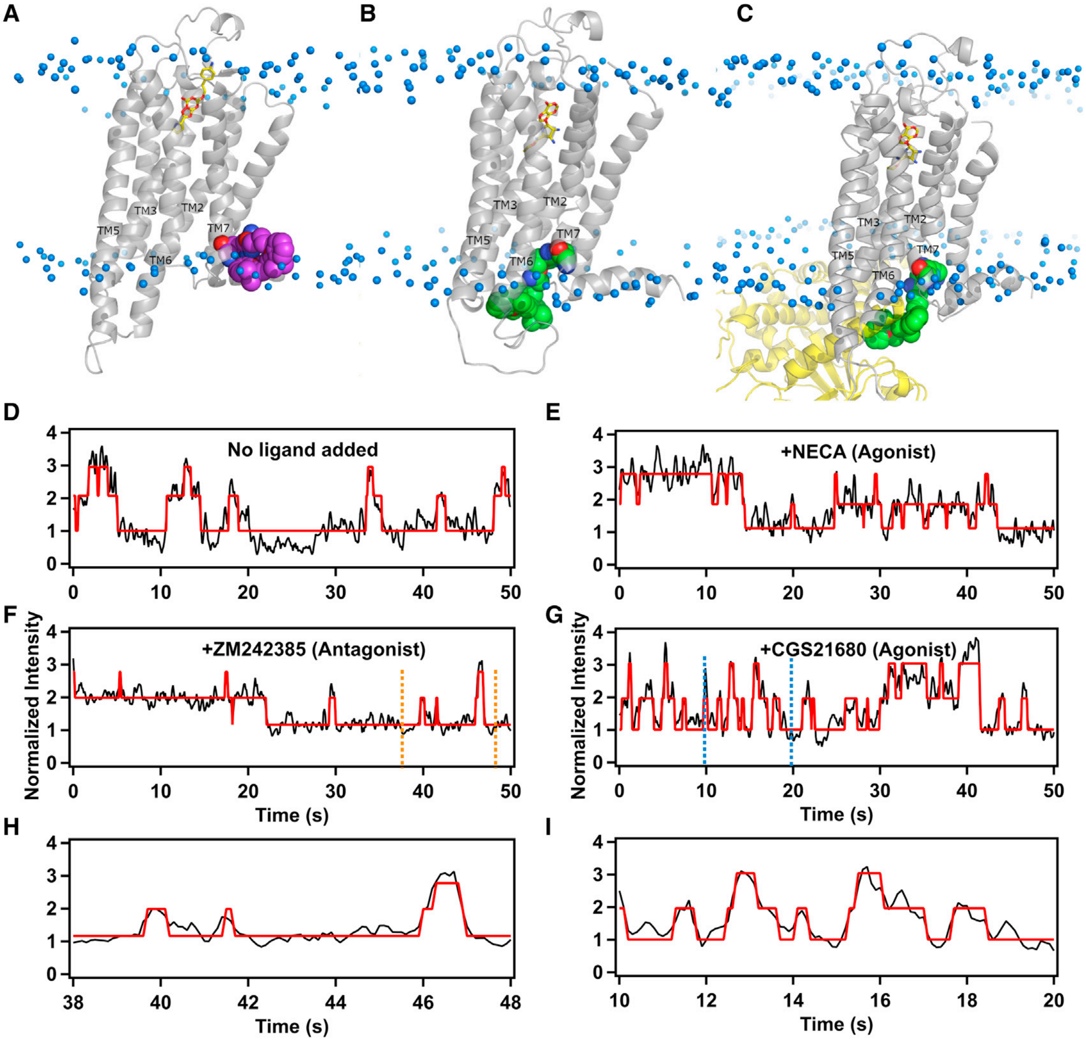

Figure 2. Structural models and representative fluorescence intensity trajectories from individual Cy3-labeled A_{2A}AR single molecules in complex with different ligands and with no ligand added (apo)

(A) A structural model of A_{2A}AR in complex with the antagonist ZM241385 is shown in gray ribbon representation. ZM241385 is shown in yellow stick representation, and the Cy3 fluorophore covalently attached to position C289 is shown in purple space-filling representation. Cy3 is positioned near the interface between the lipid bilayer and surrounding aqueous solution and is expected to exhibit a lower fluorescence emission due to a larger magnitude of conformational flexibility.

(B) A structural model of A_{2A}AR in complex with the agonist NECA is shown in gray ribbon representation. NECA is shown in yellow stick representation, and the Cy3 fluorophore covalently attached to position C289 is shown in green space-filling representation. Cy3 is located near the intracellular surface and surrounded by TMs 2, 3, 6, and 7, as well as ICL1 and ICL2, as annotated. In this position, the rate of isomerization of Cy3 fluorophore decreases, leading to an expected increase in fluorescence emission.

(C) A structural model of A_{2A}AR in a tertiary complex with the agonist NECA and G$\alpha_{S.}$ A_{2A}AR is shown in gray ribbon representation, NECA is shown in yellow stick representation, and Gα_S is shown in blue ribbon representation.

(D) A dynamic trajectory of A_{2A}AR-Cy3 without ligand added (apo). The Cy3 intensity is normalized by the mean value of the lowest intensity state. The intensity trajectories (black) are fitted by a three-state hidden Markov model (red). The trace shows a few transitions to state 3 that are very short in duration.

(E) A dynamic trajectory of the A_{2A}AR with agonist, NECA. The trace for A_{2A}AR in complex with an agonist shows more frequent transitions to a third, higher intensity state and also shows that the molecule spends a longer time in the third state as compared to traces with no ligand and antagonist (ZM241385).

(F) A dynamic trajectory of A_{2A}AR in complex with the antagonist ZM241385. Similar to the apo trace, the signal only spends a short time in state 3.

(G) A dynamic trajectory of the A_{2A}AR with agonist CGS21680. Same presentation details as in (E).

(H) An expanded view of the trajectory from 38 to 48 s from the section in panel (F), indicated by orange vertical dashed lines. The expanded view shows clear transitions between states 1 to 2 and states 2 to 3 and also shows a rare direct transition from state 3 to state 1.

(I) An expanded view of the trajectory from 10 to 20 s from the section in panel (G), marked by blue vertical dashed lines. Multiple sequential transitions between states 1 and 2 and states 2 and 3 are shown.

See also Figures S3 and S4.

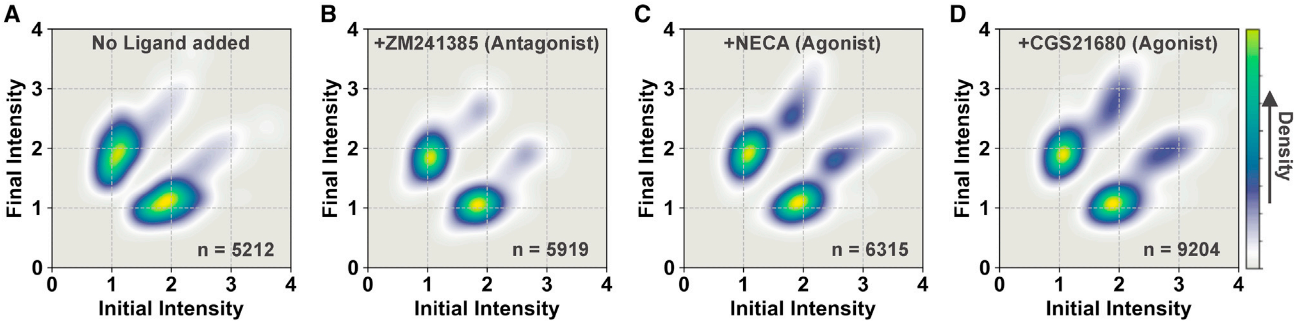

Figure 3. TDPs of $A_{2A}AR$ complexes with different ligands and without ligand

The TDPs are generated from the normalized initial and final intensities. In these plots, "n" represents the number of transitions used to prepare the TDPs. The gradient color scheme is indicated in the rightmost bar, where the arrowhead points toward a relatively higher density, which relates to the frequency of observed transitions. (A and B) The TDPs of apo and antagonist-bound $A_{2A}AR$ show that transition events predominantly occur between states 1 and 2.

(C and D) The TDPs of $A_{2A}AR$ in complexes with the agonists NECA and CGS21680 show that transition events occur between states 1 and 2 and between states 2 and 3 with measurable frequencies. No densities are observed between states 1 and 3, indicating that very few transitions occur directly between those two states.

See also Tables S1 and S2.

docking Cy3 to the sidechain of $C289^{7.54}$ and the corresponding system subjected to triplicate MD simulations, accounting for a total sampling time of 1.5 μs for each conformation. Evaluation of the trajectories included a cluster analysis of the conformations visited by the Cy3 molecule (Figure S4) and a contact map to detect and visualize potential interactions of Cy3 with nearby aromatic residues.

In all simulations of antagonist-bound $A_{2A}AR$-Cy3, Cy3 is consistently oriented toward the intracellular interface between the membrane bilayer and surrounding aqueous solution (Figure 2A) and exhibited a relatively large degree of conformational freedom, as observed in the principal component analysis (PCA) and cluster analysis (Figure S4). A larger degree of conformational freedom of the dye results in lower fluorescence emission, and thus, we assigned state 1 to the antagonist-bound conformation. This assignment is also consistent with the larger observed population of state 1 in the histograms of apo and antagonist-bound $A_{2A}AR$-Cy3 (Figures 1C and 1E).

In simulations of agonist-bound $A_{2A}AR$-Cy3, Cy3 is located in a very different environment than for apo and antagonist-bound $A_{2A}AR$-Cy3 and is observed to be surrounded by the intracellular ends of several transmembrane helices (TMs) 2, 3, 6, and 7 and intracellular loops 1 and 2 (Figure 2B). In this environment, Cy3 shows a smaller degree of conformational freedom, which would result in higher fluorescence emission. We thus assigned state 3 to the agonist-bound $A_{2A}AR$ conformation based on the significantly increased transitions to state 3 for the agonist complexes. Comparing the conformation of the dye between agonist-bound and antagonist-bound $A_{2A}AR$-Cy3, one can observe a clear dependence of the dye orientation on the global conformation of the receptor. In particular, the orientation of $C289^{7.54}$, where the dye is covalently attached, strongly depends on the backbone configuration of helix 7, which changes between inactive and active conformations of $A_{2A}AR$ (Carpenter et al., 2016; Lebon et al., 2011; Xu et al., 2011). Thus, changes in the observed intensity of Cy3 related to differences in the efficacies of bound ligands could be assigned to large conformational changes in the structure of $A_{2A}AR$-Cy3. As expected, no interconversion between structures was observed in our simulations, since the timescale of the atomistic MD simulations is orders of magnitude shorter than the timescales reported for the exchange between inactive and active conformational states (Horst et al., 2013; Sušac et al., 2018).

In MD simulations of $A_{2A}AR$-Cy3 in a tertiary complex with the agonist NECA and mini $G\alpha_S$, Cy3 shows a similar local environment, as described for the $A_{2A}AR$-Cy3 complex with NECA (Figures 2B and 2C). Based on this result, we expect that the fluorescence emission intensity of Cy3 is similar between the agonist-bound conformation and the tertiary conformation. From the above analysis, it follows that the fluorescence emission state defined as state 2 is likely not represented among currently available structures of $A_{2A}AR$.

Transitions among fluorescence intensity states occur in a reversible sequential order

Fluorescence intensities for normalized single-molecule time trajectories were fit using a three-state hidden Markov model (McKinney et al., 2006). The fitted lines are shown by the red lines in Figure 2. Results from fitting the trajectories were consistent with the intensity histograms of Figure 1. For apo $A_{2A}AR$-Cy3, the majority of molecules transitioned between two states, state 1 and state 2 (Figure S3A). A much smaller number of transitions to a higher intensity state, state 3 (Figures 2D and Table S1), was also observed but did not occur with sufficient frequency to populate the histogram (Figure 1C). The $A_{2A}AR$-Cy3 complex with the antagonist ZM241385 showed behavior similar to apo $A_{2A}AR$-Cy3, with the vast majority of transitions occurring between states 1 and 2 (Figure 2F). In contrast to these data, the $A_{2A}AR$-Cy3 complexes with agonists NECA and CGS21680 showed more frequent transitions between state 2 and state 3 (Figures 2E and 2G). For agonist-bound $A_{2A}AR$, transitions to state 3 remained in state 3 for a longer duration than for apo and antagonist-bound $A_{2A}AR$ (Figures 2E and 2G and Table S1).

To further visualize the frequencies of transitions and the connectivity of the three intensity states, we generated two-dimensional transition density plots (TDP) by using transitions from the fitted traces (Figure 3). TDPs of apo $A_{2A}AR$-Cy3 clearly showed two densities populated around normalized intensities 1 and 2 (Figure 3A), signifying frequent and prominent reversible transitions between state 1 and state 2. Similar transitions were also observed between states 1 and 2 in the TDP for the A_{2A}AR-Cy3 complex with the antagonist ZM241385 (Figure 3B).

TDPs of A_{2A}AR-Cy3 complexes with the agonists NECA and CGS21680 were significantly different from apo and antagonist-bound A_{2A}AR-Cy3 (Figure 3). In the presence of agonists, we observed that the receptor more frequently transitioned to state 3 and also spent a longer time at state 3 before returning to state 2 (Figures 3C and 3D, and Table S1). TDPs for A_{2A}AR-Cy3 complexes with the agonists NECA and CGS21680 revealed a third region with clear density at the intersection of states 2 and 3. We further analyzed the hidden Markov fitted time trajectories to quantify the relative number of sequential transitions between state 1, state 2, and state 3 (Table 2). Fewer than 2% of the total transitions occurred directly between state 1 and state 3. These rare transitions were observed for both agonist-bound and antagonist-bound A_{2A}AR; however, the addition of agonist did not increase the frequency of these rare transitions. This observation is reflected in the corresponding TDPs, which do not show measurable densities related to direct transitions between state 1 and state 3 (Figures 3C and 3D). Overall, these data indicate that for agonist-bound A_{2A}AR, transitions between state 1 and state 3 almost always proceed through state 2, which may be a potential intermediate state required for receptor activation.

DISCUSSION

We observed three distinct fluorescence emission states for agonist-bound A_{2A}AR-Cy3 (Figures 1 and 2). These distinct fluorescence emission states corresponding to different local environments of the Cy3 fluorophore bound to position 289 in helix 7 (Figures 2A–2C). The three states are also observed for the complex with the antagonist ZM241385 and the apo receptor (Figures 2F and 2D), though the population of the highest emission state for apo and antagonist-bound A_{2A}AR was too low to visualize as a significant fraction of the total population in histograms (Figure 1). MD simulations of A_{2A}AR-Cy3 indicate that due to steric hindrances, the fluorophore cannot change local environments without larger structural rearrangements of the receptor (Figures 2A–2C). Thus, the different emission states likely correlate with backbone rearrangements of the A_{2A}AR TMs at the intracellular surface.

The observation of three distinct states is interesting when compared with earlier single-molecule fluorescence studies of the β_2-adrenergic receptor, where two conformational states were observed in single-color TIRF experiments that used a similar experimental design as the present study (Lamichhane et al., 2015, 2020). Two conformational states were also reported in single-molecule FRET experiments (Gregorio et al., 2017). The different number of observed emission states between A_{2A}AR and β_2AR suggests potential differences in mechanisms of activation and indicates that further investigations of many more different class A GPCRs are needed to develop a more general understanding of GPCR function-related conformational dynamics.

Results from the hidden Markov analysis revealed a correlation between the frequency of transitions between state 2 and state 3 and ligand efficacy. Relative to the apo receptor, we observed the number of molecules transitioning between states 2 to 3 increased significantly for complexes with agonists and did not significantly change for complexes with antagonists (Table S2). Intriguingly, the hidden Markov analysis also showed only a slight correlation between ligand efficacy and frequency of transitions between states 1 and 2 (Table S2). Taken together, these results suggest the possibility of subtle differences in the conformation of state 2 for antagonist complexes and for agonist complexes that may not be visible at the intracellular surface of the protein but are related to different frequencies of transitions to state 3.

In the present study, the integration time of the camera used for data acquisition was 100 ms, so fluctuations in the fluorescence intensity must occur on timescales equal to or slower than 100 ms to be observed, corresponding to rates of exchange processes on the order of 10 s^{-1} or slower. These relatively slower processes are in line with rates of exchange between different conformational states measured in ^{19}F-NMR experiments of A_{2A}AR in detergent micelles containing n-Dodecyl-b-D-Maltopyranoside (DDM) and cholesteryl hemisuccinate (CHS) (Sušac et al., 2018). These slower rates are also in line with rates of slow conformational exchange in β_2AR estimated by ^{19}F-NMR to be $k_{ex} \leq 10\ s^{-1}$ (Horst et al., 2013). MD simulations in the present work could detect two different conformational states of A_{2A}AR-Cy3 but are not sufficiently long to detect these slow transitions between different conformational states observed in single-molecule fluorescence data.

The present work complements other recent single-molecule studies of A_{2A}AR that measured dynamic processes on relatively faster timescales. In a recent report of single-molecule FRET of A_{2A}AR in detergent micelles containing LMNG and CHS, ligand-depending shifts and broadening of smFRET distributions were interpreted to suggest exchange between inactive and active conformations of A_{2A}AR that occurred on a timescale of $\sim$3 ms or $k_{ex} \geq \sim 30–40\ s^{-1}$ (Fernandes et al., 2021). In a separate study, Maslov et al. reported observations of exchange processes on a similar timescale of sub-millisecond to low millisecond fluctuations with A_{2A}AR in nanodiscs containing POPC and POPG lipids (Maslov et al., 2020). Both the Fernandes et al. and Maslov et al. studies utilized a diffusion-based experimental design in which the observation of FRET signals depends on the rate of diffusion of the receptors in aqueous solutions. This design would not permit observations of exchange processes with rates that are reported here. With the TIRF experimental design, molecules are tethered to the microscope slide, which allows one to monitor dynamics on relatively longer timescales. The relatively faster dynamics reported by Fernandes and Maslov may have also occurred with A_{2A}AR samples in the present study but were not observed due to limitations of the time resolution of the camera.

One of the more surprising observations of this work is the reversible temporal ordering of the fluorescence emission states (Figure 4). This observation is reminiscent of single-molecule FRET data from a recent study of a class C GPCR dimer, where receptor monomers were labeled with different fluorophores, and FRET measurements were recorded between each monomer in a functional dimer (Liauw et al., 2021). In Liauw et al., FRET data were interpreted as evidence of “conformational

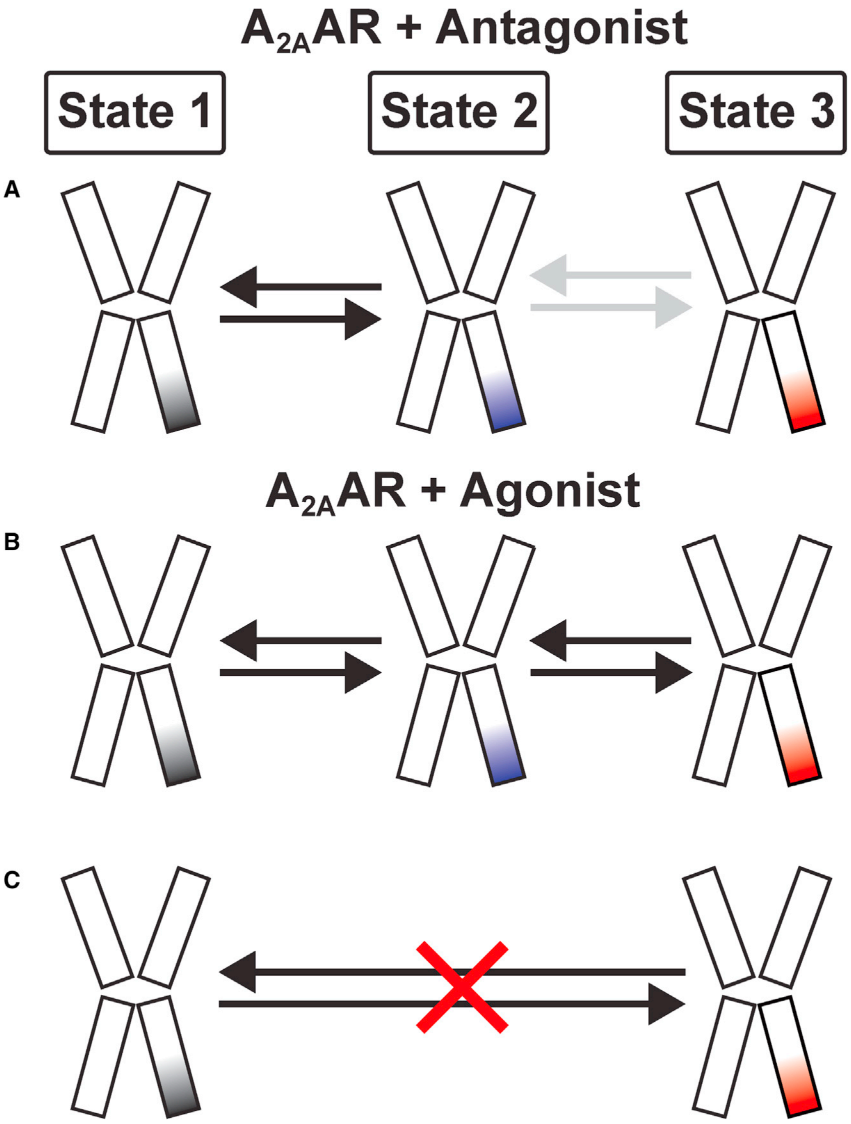

Figure 4. Schematic of the temporal ordering observed for transitions among $A_{2A}AR$ conformational states

For each receptor cartoon representation, the color of the rightmost intracellular helix corresponds to the color scheme used with the histograms shown in Figure 2 panels C–F. (A) For apo $A_{2A}AR$ and antagonist-bound $A_{2A}AR$, transitions are predominantly observed between states 1 and 2, indicated by the black arrows. Far fewer transitions are observed between states 2 and 3, indicated by the gray arrows.

(B) For agonist-bound $A_{2A}AR$, transitions are observed between states 1 and 2 and between states 2 and 3 (black arrows).

(C) Transitions directly between states 1 and 3 are only very rarely observed, as indicated by the red "X".

checkpoints" that suggested an activation process involving stepwise interactions between monomers in the homodimer (Liauw et al., 2021). Here, we observed a stepwise process involving conformational changes within a class A GPCR monomer. This observation creates a distinct framework for understanding GPCR activation processes and for resolving questions in future studies of how orthosteric ligands, allosteric modulators, and mutations may potentially alter the order of these exchange processes.

STAR★METHODS

Detailed methods are provided in the online version of this paper and include the following:

- KEY RESOURCES TABLE
- RESOURCE AVAILABILITY
  - Lead contact
  - Materials availability
  - Data and code availability
- EXPERIMENTAL MODEL AND SUBJECT DETAILS
  - Microbes
  - Cell lines
- METHOD DETAILS
  - Mutagenesis
  - MSP1D1 expression and purification
  - $A_{2A}AR$ Production
  - $A_{2A}AR$ purification
  - Single-molecule fluorescence sample preparation
  - Radioligand binding assays for $A_{2A}AR$ in lipid nanodiscs
  - Single-molecule fluorescence data acquisition
  - Molecular dynamics simulations
- QUANTIFICATION AND STATISTICAL ANALYSIS
  - Single-molecule fluorescence data analysis
  - Quantification and analysis of ligand binding for $A_{2A}AR$ in lipid nanodiscs

SUPPLEMENTAL INFORMATION

Supplemental information can be found online at https://doi.org/10.1016/j.str.2021.11.005.

ACKNOWLEDGMENTS

This work was supported by the National Institutes of Health, R35 GM142946 (R. L.) and the start-up funds from the College of Arts and Sciences, University of Tennessee, Knoxville (R. L.). This research was funded by the National Institutes of Health, R35 GM138291 (M.T.E., N.T., A.P.R., and B.J.), DA048353 (L.R.M. and C.R.M.), and DA047855 (L.R.M. and C.R.M.), and a Ralphe E. Powe Junior Faculty Award from Oak Ridge Affiliated Universities (M.T.E). The simulations were conducted in the resources of the Swedish National Supercomputing Centers (SNIC). We thank Raymond Pauszek from The Scripps Research Institute for providing custom software to prepare the TDPs.

AUTHOR CONTRIBUTIONS

R.L. and M.T.E. initiated the project and designed the experiments; R.L., M.T.E., S.W., N.T., and A.P.R. conducted the experiments; H.G.dT. performed and analyzed simulations; R.L. and S.W. analyzed the fluorescence imaging data with input from M.T.E.; S.O. conducted the radioligand binding experiments with input from L.R.M. and C.R.M.; M.T.E. and R.L. wrote the manuscript with input from all co-authors.

DECLARATION OF INTERESTS

H.G.dT. is a co-founder and stock holder of MODSIM Pharma AB.

Received: June 4, 2021
Revised: September 26, 2021
Accepted: November 17, 2021
Published: December 10, 2022

REFERENCES

Aviram, H.Y., Pirchi, M., Barak, Y., Riven, I., and Haran, G. (2018). Two states or not two states: single-molecule folding studies of protein L. J. Chem. Phys. *148*, 123303.

Bayburt, T.H., and Sligar, S.G. (2010). Membrane protein assembly into Nanodiscs. FEBS Lett. *584*, 1721–1727.

Berendsen, H.J., Postma, J.P., van Gunsteren, W.F., and Hermans, J. (1981). Interaction models for water in relation to protein hydration. In Intermolecular Forces (Springer), pp. 331–342.

Berezhna, S.Y., Gill, J.P., Lamichhane, R., and Millar, D.P. (2012). Single-molecule Förster resonance energy transfer reveals an innate fidelity checkpoint in DNA polymerase I. J. Am. Chem. Soc. *134*, 11261–11268.

Berger, O., Edholm, O., and Jähnig, F. (1997). Molecular dynamics simulations of a fluid bilayer of dipalmitoylphosphatidylcholine at full hydration, constant pressure, and constant temperature. Biophys. J. *72*, 2002–2013.

Bostock, M.J., Solt, A.S., and Nietlispach, D. (2019). The role of NMR spectroscopy in mapping the conformational landscape of GPCRs. Curr. Opin. Struct. Biol. *57*, 145–156.

Carpenter, B., Nehmé, R., Warne, T., Leslie, A.G.W., and Tate, C.G. (2016). Structure of the adenosine A2A receptor bound to an engineered G protein. Nature *536*, 104–107.

Chakrabarti, N., Neale, C., Payandeh, J., Pai, E.F., and Pomès, R. (2010). An ris-like mechanism ofpPore dilation in the corA magnesium transport tystem. Biophys. J. *98*, 784–792.

Cheng, Y.-C., and Prusoff, W.H. (1973). Relationship between the inhibition constant (Ki) and the concentration of inhibitor which causes 50 per cent inhibition (I50) of an enzymatic reaction. Biochem. Pharmacol. *22*, 3099–3108.

Chung, H.S., McHale, K., Louis, J.M., and Eaton, W.A. (2012). Single-molecule fluorescence experiments determine protein folding transition path times. Science *335*, 981–984.

Clark, L.D., Dikiy, I., Chapman, K., Rödström, K.E., Aramini, J., LeVine, M.V., Khelashvili, G., Rasmussen, S.G., Gardner, K.H., and Rosenbaum, D.M. (2017). Ligand modulation of sidechain dynamics in a wild-type human GPCR. Elife *6*, e28505.

Dodda, L.S., Cabeza de Vaca, I., Tirado-Rives, J., and Jorgensen, W.L. (2017). LigParGen web server: an automatic OPLS-AA parameter generator for organic ligands. Nucleic Acids Res. *45*, W331–W336.

Eddy, M.T., Gao, Z.-G., Mannes, P., Patel, N., Jacobson, K.A., Katritch, V., Stevens, R.C., and Wüthrich, K. (2018). Extrinsic tryptophans as NMR probes of allosteric coupling in membrane proteins: application to the A2A adenosine receptor. J. Am. Chem. Soc. *140*, 8228–8235.

Eddy, M.T., Lee, M.-Y., Gao, Z.-G., White, K.L., Didenko, T., Horst, R., Audet, M., Stanczak, P., McClary, K.M., Han, G.W., et al. (2017). Allosteric coupling of drug binding and intracellular signaling in the A2A adenosine receptor. Cell *172*, 68–80.

Eddy, M.T., Martin, B.T., and Wüthrich, K. (2021). A2A adenosine receptor partial agonism related to structural rearrangements in an activation microswitch. Structure *29*, 170–176.e3.

Esguerra, M., Siretskiy, A., Bello, X., Sallander, J., and Gutiérrez-de-Terán, H. (2016). GPCR-ModSim: a comprehensive web based solution for modeling G-protein coupled receptors. Nucleic Acids Res. *44*, W455–W462.

Fernandes, D.D., Neale, C., Gomes, G.-N.W., Li, Y., Malik, A., Pandey, A., Orazietti, A.P., Wang, X., Ye, L., Scott Prosser, R., et al. (2021). Ligand modulation of the conformational dynamics of the A2A adenosine receptor revealed by single-molecule fluorescence. Sci. Rep. *11*, 5910–5916.

Gregorio, G.G., Masureel, M., Hilger, D., Terry, D.S., Juette, M., Zhao, H., Zhou, Z., Perez-Aguilar, J.M., Hauge, M., Mathiasen, S., et al. (2017). Single-molecule analysis of ligand efficacy in β2AR–G-protein activation. Nature *547*, 68–73.

Gutiérrez-de-Terán, H., Massink, A., Rodríguez, D., Liu, W., Han, G.W., Joseph, J.S., Katritch, I., Heitman, L.H., Xia, L., IJzerman, A.P., et al. (2013). The role of a sodium ion binding site in the allosteric modulation of the A2A adenosine G protein-coupled receptor. Structure *21*, 2175–2185.

Hagn, F., Nasr, M.L., and Wagner, G. (2018). Assembly of phospholipid nanodiscs of controlled size for structural studies of membrane proteins by NMR. Nat. Protoc. *13*, 79–98.

Hauser, A.S., Attwood, M.M., Rask-Andersen, M., Schiöth, H.B., and Gloriam, D.E. (2017). Trends in GPCR drug discovery: new agents, targets and indications. Nat. Rev. Drug Discov. *16*, 829–842.

Hess, B., Bekker, H., Berendsen, H.J.C., and Fraaije, J.G.E.M. (1997). LINCS: a linear constraint solver for molecular simulations. J. Comput. Chem. *18*, 1463–1472.

Hess, B., Kutzner, C., van der Spoel, D., and Lindahl, E. (2008). GROMACS 4:algorithms for highly efficient ,load -Balanced,and scalable molecular simulation. J. Chem. Theor. Comput. *4*, 435–447.

Hoover, W. (1985). Canonical dynamics: equilibrium phase-space distributions. Phys.Rev. A *31*, 1695–1697.

Horst, R., Liu, J.J., Stevens, R.C., and Wüthrich, K. (2013). β_2-adrenergic receptor activation by agonists studied with ^{19}F NMR spectroscopy. Angew. Chem. *52*, 10762–10765.

Huang, S.K., Pandey, A., Tran, D.P., Villanueva, N.L., Kitao, A., Sunahara, R.K., Sljoka, A., and Prosser, R.S. (2021). Delineating the conformational landscape of the adenosine A2A receptor during G protein coupling. Cell *184*, 1884–1894.e14.

Hwang, H., Kim, H., and Myong, S. (2011). Protein induced fluorescence enhancement as a single molecule assay with short distance sensitivity. Proc. Natl. Acad. Sci. U S A *108*, 7414–7418.

Kim, J.-Y., and Chung, H.S. (2020). Disordered proteins follow diverse transition paths as they fold and bind to a partner. Science *368*, 1253–1257.

Lamichhane, R., Liu, J.J., Pljevaljcic, G., White, K.L., van der Schans, E., Katritch, V., Stevens, R.C., Wuthrich, K., and Millar, D.P. (2015). Single-molecule view of basal activity and activation mechanisms of the G protein-coupled receptor β_2AR. Proc. Natl. Acad. Sci. U S A *112*, 14254–14259.

Lamichhane, R., Liu, J.J., White, K.L., Katritch, V., Stevens, R.C., Wuthrich, K., and Millar, D.P. (2020). Biased signaling of the G-protein-coupled receptor β_2AR is governed by conformational exchange kinetics. Structure *28*, 371–377.e3.

Lamichhane, R., Solem, A., Black, W., and Rueda, D. (2010). Single-molecule FRET of protein-nucleic acid and protein-protein complexes: surface passivation and immobilization. Methods *52*, 192–200.

Lebon, G., Warne, T., Edwards, P.C., Bennett, K., Langmead, C.J., Leslie, A.G.W., and Tate, C.G. (2011). Agonist-bound adenosine A2A receptor structures reveal common features of GPCR activation. Nature *474*, 521–525.

Leitz, A.J., Bayburt, T.H., Barnakov, A.N., Springer, B.A., and Sligar, S.G. (2006). Functional reconstitution of Beta2-adrenergic receptors utilizing self-assembling Nanodisc technology. Biotechniques *40*, 601–602, 604, 606, passim.

Liauw, B.W.-H., Afsari, H.S., and Vafabakhsh, R. (2021). Conformational rearrangement during activation of a metabotropic glutamate receptor. Nat. Chem. Biol. *17*, 291–297.

Liu, W., Chun, E., Thompson, A.A., Chubukov, P., Xu, F., Katritch, V., Han, G.W., Roth, C.B., Heitman, L.H., IJzerman, A.P., et al. (2012). Structural basis for allosteric regulation of GPCRs by sodium ions. Science *337*, 232–236.

Maslov, I., Volkov, O., Khorn, P., Orekhov, P., Gusach, A., Kuzmichev, P., Gerasimov, A., Luginina, A., Coucke, Q., Bogorodskiy, A., et al. (2020). Sub-millisecond conformational dynamics of the A2A adenosine receptor revealed by single-molecule FRET. bioRxiv, 2020.2011.2026.400184.

McGibbon, R.T., Beauchamp, K.A., Harrigan, M.P., Klein, C., Swails, J.M., Hernández, C.X., Schwantes, C.R., Wang, L.-P., Lane, T.J., and Pande, V.S. (2015). MDTraj: a modern open library for the analysis of molecular dynamics trajectories. Biophys. L. *109*, 1528–1532.

McKinney, S.A., Joo, C., and Ha, T. (2006). Analysis of single-molecule FRET trajectories using hidden Markov modeling. Biophys. J. *91*, 1941–1951.

Mizumura, T., Kondo, K., Kurita, M., Kofuku, Y., Natsume, M., Imai, S., Shiraishi, Y., Ueda, T., and Shimada, I. (2020). Activation of adenosine A2A receptor by lipids from docosahexaenoic acid revealed by NMR. Sci. Adv. *6*, eaay8544.

Nosé, S. (1984). A unified formulation of the constant temperature molecular dynamics methods. J. Chem. Phys. *81*, 511–519.

Pauszek, R.F., III, Lamichhane, R., Singh, A.R., and Millar, D.P. (2021). Single-molecule view of coordination in a multi-functional DNA polymerase. Elife *10*, e62046.

Robertson, M.J., Tirado-Rives, J., and Jorgensen, W.L. (2015). Improved peptide and protein torsional energetics with the OPLSAA force field. J. Chemf Theor. Comput. *11*, 3499–3509.

Rouck, J.E., Krapf, J.E., Roy, J., Huff, H.C., and Das, A. (2017). Recent advances in nanodisc technology for membrane protein studies (2012-2017). FEBS Lett. *591*, 2057–2088.

Sastry, G.M., Adzhigirey, M., Day, T., Annabhimoju, R., and Sherman, W. (2013). Protein and ligand preparation: parameters, protocols, and influence on virtual screening enrichments. J. Comput. Aided Mol. Des. *27*, 221–234.

Schrodinger, L.L.C. (2015). The PyMOL Molecular Graphics System, version 1.8.

Schrödinger, L. (2021). Macromodel.

Schuler, B., Lipman, E.A., and Eaton, W.A. (2002). Probing the free-energy surface for protein folding with single-molecule fluorescence spectroscopy. Nature *419*, 743–747.

Shimada, I., Ueda, T., Kofuku, Y., Eddy, M.T., and Wüthrich, K. (2019). GPCR drug discovery: integrating solution NMR data with crystal and cryo-EM structures. Nat. Rev. Drug Discov. *18*, 59–82.

Stefanski, K.M., Russell, C.M., Westerfield, J.M., Lamichhane, R., and Barrera, F.N. (2021). PIP2 promotes conformation-specific dimerization of the EphA2 membrane region. J. Biol. Chem. *296*, 100149.

Stennett, E.M., Ciuba, M.A., Lin, S., and Levitus, M. (2015). Demystifying PIFE: the photophysics behind the protein-induced fluorescence enhancement phenomenon in cy3. J. Phys. Chem. Lett. *6*, 1819–1823.

Sušac, L., Eddy, M.T., Didenko, T., Stevens, R.C., and Wüthrich, K. (2018). A2A adenosine receptor functional states characterized by 19F-NMR. Proc. Natl. Acad. Sci. U S A *115*, 12733–12738.

Wagner, G., DeMarco, A., and Wüthrich, K. (1976). Dynamics of the aromatic amino acid residues in the globular conformation of the basic pancreatic trypsin inhibitor (BPTI). Biophys. Struct. Mech. *2*, 139–158.

Wüthrich, K., and Wagner, G. (1975). NMR investigations of the dynamics of the aromatic amino acid residues in the basic pancreatic trypsin inhibitor. FEBS Lett. *50*, 265–268.

Xu, F., Wu, H., Katritch, V., Han, G.W., Jacobson, K.A., Gao, Z.-G., Cherezov, V., and Stevens, R.C. (2011). Structure of an agonist-bound human A2A adenosine receptor. Science *332*, 322–327.

Ye, L., Neale, C., Sljoka, A., Lyda, B., Pichugin, D., Tsuchimura, N., Larda, S.T., Pomès, R., García, A.E., Ernst, O.P., et al. (2018). Mechanistic insights into allosteric regulation of the A2A adenosine G protein-coupled receptor by physiological cations. Nat. Comm. *9*, 1372.

Ye, L., Van Eps, N., Zimmer, M., Ernst, O.P., and Prosser, R.S. (2016). Activation of the A2A adenosine G-protein-coupled receptor by conformational selection. Nature *533*, 265–268.

STAR★METHODS

KEY RESOURCES TABLE

REAGENT or RESOURCE	SOURCE	IDENTIFIER
Antibodies		
Monoclonal ANTI-FLAG® M2-Alkaline Phosphatase antibody produced in mouse	Sigma-Aldrich	Cat#A9469; RRID: AB_439699
Bacterial and virus strains		
XL10-Gold ultracompetent cells	Agilent	Cat#200314
BL21 DE3 cells	Agilent	Cat#200132
Chemicals, peptides, and recombinant proteins		
n-Dodecyl-b-D-Maltopyranoside (DDM)	Anatrace	Cat#D310
Cholesteryl hemisuccinate (CHS)	Sigma-Aldrich	Cat#C6512
Adenosine 5′-triphosphate disodium salt hydrate (ATP)	Sigma-Aldrich	Cat#A2383
DPN I	NEB	Cat#R0176S
YNB (without amino acids and ammonium salts)	RPI	Cat#Y20060
Biotin	Sigma-Aldrich	Cat#B4639
4-(2-[7-Amino-2-(2-furyl)[1,2,4]triazolo[2,3-a][1,3,5]triazin-5-ylamino]ethyl)phenol (ZM241385)	Tocris	Cat#1036
5′-N-Ethylcarboxamidoadenosine (NECA)	Tocris	Cat#1691
Xanthine amine congener (XAC)	Tocris	Cart#3200
4-[2-[[6-Amino-9-(N-ethyl-b-D-ribofuranuronamidosyl)-9H-purin-2-yl] amino]ethyl]benzenepropanoic acid hydrochloride (CGS21680)	Tocris	Cat#1063
Theophylline	Sigma-Aldrich	Cat#T1633
[3H]4-[2-[7-amino-2-(2-furyl)-1,2,4-triazolo [1,5-a][1,3,5]triazin-5-yl-amino]ethylphenol ([3H]ZM241385)	American Radiolabeled Chemicals	Cat#ART0884-50
TALON Metal affinity resin	Gold bio	Cat#H-310-5
1-Palmitoyl-2-oleoyl-glycero-3-phosphocholine (POPC)	Avanti	SKU#850457
1-Palmitoyl-2-oleoyl-sn-glycero-3-phospho-L-serine (sodium salt) (POPS)	Avanti	SKU#840034
1,2-Dipalmitoyl-sn-glycero-3-phosphoethanolamine-N-(cap biotinyl) (sodium salt)	Avanti	SKU#870277
Cholic acid, sodium salt	Anatrace	Cat#S1010S
Isopropyl β- d-1-thiogalactopyranoside (IPTG)	Goldbio	Cat#I2481C
Triton X-100	Sigma-Aldrich	Cat#T8787
SnakeSkin™ dialysis tubing, 10K MWCO, 22 mm	ThermoFischer Scientific	Cat#68100
Bio-beads SM-2 Adosrbents	Biorad	Cat#1523920
Glucose oxidase	Sigma-Aldrich	Cat# G2133
Streptavidin	Thermo Fisher	Cat# S888
Cy3 maleimide,	GE Healthcare	PA23031
mPEG-SVA, MW 5,000	Laysan Bio	M-SVA
Biotin-PEG-SVA, MW 5,000	Laysan Bio	BIO-SVA
Catalase from bovine liver	Sigma-Aldrich	Cat# C100

(*Continued on next page*)

Continued

REAGENT or RESOURCE	SOURCE	IDENTIFIER
Deposited data		
Thermostabilized A_{2A}AR in complex with NECA	Lebon et al., (2011)	PDB:2YDV
A_{2A}AR in complex with NECA bound to an engineered G protein	Carpenter et al., (2016)	PDB:5G53
A_{2A}AR-BRIL bound to ZM241385	Liu et al., (2012)	PDB:4EIY
Experimental models: Organisms/strains		
P. pastoris: Bg12	BioGrammatics	Cat#PS004-01
Oligonucleotides		
A_{2A}AR_A289C_F:TCGGTTGTGAATCCC TTCATTTACTGCTACCGTATCCGCGAG TTCCGCCAG	This study	n/a
A_{2A}AR_A289C_R:CTGGCGGAAC TCGCGGATACGGTAGCAGTAAA TGAAGGGATTCACAACCGA	This study	n/a
Recombinant DNA		
Plasmid: human A_{2A}AR (1-316) in pPIC9K	Eddy et al., (2018)	n/a
Plasmid: human A_{2A}AR[A289C]	This study	n/a
Software and algorithms		
GraphPad prism	GraphPad Software Inc.	https://www.graphpad.com
PyMOL	Pymol.org	https://pymol.org/2/
GROMACS	Gromacs.org	https://www.gromacs.org/
Maestro	Schrodinger	https://www.schrodinger.com/products/maestro
IDL	l3harrisgeospatial.com, Version 8.7	https://www.l3harrisgeospatial.com
HaMMy	McKinney et al. (2006)	https://ha.med.jhmi.edu/resources
Igor Pro	Wavemetrics.com	https://www.wavemetrics.com/downloads
Single software	Ha Lab	https://ha.med.jhmi.edu/resources
Other		
PD-10 column	Cytiva	Cat#17085101
Vivaspin 20 ultrafiltration spin columns 30 kDa MWCO	Cytiva	Cat#28932361

RESOURCE AVAILABILITY

Lead contact

Lead Contact: Dr. Rajan Lamichhane (rajan@utk.edu). Further information and requests for resources or reagents should be directed to and will be fulfilled by the Lead Contact.

Materials availability

All unique reagents generated in this study are available from the Lead Contact by request and with a completed Materials Transfer Agreement.

Data and code availability

All data reported in this paper will be shared by the lead contact upon request.

This paper does not report original code.

Any additional information required to reanalyze the data reported in this paper is available from the lead contact upon request.

EXPERIMENTAL MODEL AND SUBJECT DETAILS

Microbes

XL-10 *E. coli* cells were cultured in LB media, BL21(DE3) cells were cultured in TB media, and the BG12 strain of *P. pastoris* was cultured in BMGY and BMMY media.

Cell lines

All cell lines used in this study were authenticated by the suppliers and were chosen to remain consistent with previous studies.

METHOD DETAILS

Mutagenesis

PCR-based site-directed mutagenesis (QuickChange II, Strategene, CA) was used to generate the A_{2A}AR A289C variant used for single-molecule fluorescence experiments. Primers used for this effort are provided in the key resources table.

MSP1D1 expression and purification

MSP1D1 was expressed and purified similar to protocols described in previous studies (Bayburt and Sligar, 2010; Hagn et al., 2018). MSP1D1 encoded in the open reading frame of a pET28a vector (Invitrogen) was transformed into the BL21(DE3) *E. coli* strain. A single transformed colony was inoculated into 5 mL Luria–Bertani (LB) broth containing 50 mg/mL kanamycin and incubated overnight at 37°C with shaking. 1L Terrific Broth (TB) media was inoculated with the overnight culture and allowed to reach an optical density of 0.6-0.8, and protein expression was induced with 1 mM isopropyl β-D-1-thiogalactopyranoside (IPTG) and allowed to proceed for 4 hours at 37°C. The cells were harvested by centrifugation at 4000 × g for 30 min, frozen in liquid nitrogen and stored at −80°C for later use. The cell pellets were thawed and resuspended in lysis buffer (50 mM Tris-HCl, pH 8.0, 500 mM NaCl, 1% Triton X-100, and 1 mM EDTA) at 20 mL of buffer per gram of cell pellet and 100 μL of in-house prepared protease inhibitor solution was added. The resuspended cells were lysed with a single pass through a cell disruptor (Pressure Biosciences) operating at 20,000 psi. Insoluble material was separated by ultracentrifugation at 20,000 × g at 4°C for 45 minutes, and the supernatant was applied to a Ni-NTA column equilibrated with 50 mM Tris-HCl, pH 8.0, 500 mM NaCl, and 1% (w/v) Triton X-100. The column was washed with 5 CV of wash buffer 1 (50 mM Tris-HCl, pH 8.0, 500 mM NaCl, and 1% (w/v) Triton X-100), washed with 5 CV of buffer 2 (50 mM Tris-HCl, pH 8.0, 500 mM NaCl, and 50 mM cholate), washed with 5 CV of buffer 3 (50 mM Tris-HCl, pH 8.0, and 500 mM NaCl) and washed with 5 CV of buffer 4 (50 mM Tris-HCl, pH 8.0, 500 mM NaCl, and 20 mM imidazole). MSP1D1 was eluted with 5 CV of buffer containing 50 mM Tris-HCl, pH 8.0, 500 mM NaCl, and 500 mM imidazole. Fractions containing MSP1D1 were pooled and dialyzed against 50 mM Tris-HCl, pH 8.0, 20 mM NaCl and 0.5 mM EDTA in dialysis tubing with a 10 kDa MWCO (Thermo-Fisher Scientific). MSP1D1 was then incubated with TEV protease at a 1:100 (TEV: MSP) molar ratio overnight at 4°C. The protein solution was applied to a nickel column and the flow-through fraction containing purified MSP1D1 was collected. MSP1D1 was then transferred into a storage buffer containing 20 mM Tris, pH 7.5, 100 mM NaCl, and 0.5 mM EDTA by dialysis for 4 hours using dialysis tubing with a 10 kDa MWCO (Thermo-Fisher Scientific). MSP1D1 was concentrated to 1 mM, frozen in liquid nitrogen and stored at −80 °C for future use.

A_{2A}AR Production

The gene encoding human A_{2A}AR(1–-316) containing a point mutation to remove the only glycosylation site (N154Q), an N-terminal FLAG tag, and a 10 X C-terminal His tag was cloned into a pPIC9K vector (Invitrogen) at the BamHI and NotI restriction sites. Alanine 289 was replaced with cysteine via site-directed mutagenesis, and the resulting plasmid was introduced by electroporation into the BG12 strain of *Pichia pastoris* (Biogrammatics). Transformed colonies were screened for optimal protein expression using a previously reported Western blot assay (Eddy et al., 2017) that utilizes an anti-FLAG monoclonal conjugated antibody to identify high-expressing clones. Once identified, glycerol stocks were prepared from high-expressing clones and stored at −80°C. Small scale cultures containing 4 mL buffered minimal glycerol (BMGY) media in 15 mL culture tubes were inoculated from the glycerol stock and grown at 30°C for 48 hours to reach an optical density of 9-10. These cultures were then used to inoculate 50 mL BMGY medium in a 250 mL baffled flask and incubated at 30°C for approximately 60 hours to reach an optical density of 15–20. Subsequently, 2.8 L baffled flasks containing 500 mL BMGY media were inoculated with the 50 mL cultures and incubated at 30°C for 48 h to reach an optical density of 15-20. Cells were collected by centrifugation at 3000 × g for 15 minutes and resuspended in 500 mL of buffered minimal methanol (BMMY) medium without methanol and the temperature was lowered to 28°C. These cultures were incubated for 6 hours to ensure complete metabolic digest of glycerol before methanol was added to a final concentration of 0.5% w/v to induce protein expression. Two additional 0.5% w/v aliquots of methanol were added at 12 hour intervals after initial induction. Expression proceeded for a total of 36 hours and then cells were harvested by centrifugation at 3000 × g for 15 minutes. The isolated cell pellets were frozen in liquid nitrogen and stored at −80°C for later purification.

A_{2A}AR purification

Cell pellets containing A_{2A}AR were resuspended in lysis buffer (50 mM sodium phosphate pH 7.0, 100 mM NaCl, 5% glycerol (w/v), and in-house prepared protease inhibitor solution) and lysed by a single pass through a cell disruptor (Pressure Biosciences) operating at 40,000 psi. Membranes were isolated and collected by ultracentrifugation at 200,000 × g, frozen in liquid nitrogen and stored at −80°C for future use. Isolated membrane pellets were resuspended in buffer (10 mM HEPES pH 7.0, 10 mM KCl, 20 mM $MgCl_2$, 1M NaCl) and treated with 1 mM theophylline and protease inhibitor solution for 1 hour. Subsequently, protein was extracted from the membrane in buffer containing 0.5% (w/v) n-Dodecyl-β-D-Maltopyranoside (DDM), 0.05% cholesteryl hemisuccinate (CHS), 50 mM HEPES pH 7.0, and 500 mM NaCl for 6 hours at 4°C. Then insolubilized material was separated by ultracentrifugation at 200,000 × g for 30 min, and the supernatant was collected and incubated overnight at 4°C with Co^{2+}-charged affinity resin (Talon, Takara Bio USA) and 30 mM imidazole. The resin was then washed with 20 CV of wash buffer 1 (50 mM HEPES pH 7.0, 500 mM NaCl, 10 mM $MgCl_2$, 30 mM imidazole, 8 mM ATP, 0.05% DDM, and 0.005% CHS). Resin was collected and washed 2 more times with 20 CV of wash buffer 2 (25 mM HEPES pH 7.0, 250 mM NaCl, 5% glycerol, 30 mM imidazole, 0.05% DDM, 0.005% CHS, and ligand), and eluted with buffer 3 (50 mM HEPES pH 7.0, 250 mM NaCl, 5% glycerol, 300 mM imidazole, 0.05% DDM, 0.005% CHS, and ligand). After elution, the protein was exchanged into a final buffer (25 mM HEPES pH 7.0, 75 mM NaCl, 0.05% DDM, 0.005% CHS, and ligand), using a PD-10 desalting column (Cytiva). All buffers were prepared with a saturating concentration of the required ligand. Apo protein was purified without addition of ligand to the sample preparation buffers.

Single-molecule fluorescence sample preparation

Assembly of nanodiscs followed protocols adapted from previous studies (Bayburt and Sligar, 2010; Hagn et al., 2018) that were further optimized for experiments with $A_{2A}AR$. Purified $A_{2A}AR$ was mixed with purified MSP1D1 and lipids solubilized in buffer (25 mM Tris pH 8.0, 150 mM NaCl and 200 mM sodium cholate) in a molar ratio of 1:5:250 ($A_{2A}AR$:MSP1D1:lipids). Lipids were mixed in a molar ratio of 65:30:5 (POPC:POPS:biotin-POPE) prior to mixing with $A_{2A}AR$ and MSP1D1. The mixture of $A_{2A}AR$, MSP1D1 and lipids was incubated for 4 hours at 4°C. Subsequently, bio-beads (Bio-Rad Laboratories) were added to the mixture and incubated overnight at 4°C. The bio-beads were then removed and the resulting mixture was incubated with Ni-NTA resin (GoldBio) for 24 hours at 4°C. After overnight incubation, a 10 fold molar excess of the Cy3 maleimide fluorophore (GE Healthcare) was added to the mixture and incubated in the dark at 4°C for 3 h. The resin was then washed with 2 CV of a wash buffer (50 mM HEPES, pH 7.0, 150 mM NaCl and 10 mM imidazole), and nanodiscs containing $A_{2A}AR$ were eluted with buffer (50 mM HEPES, pH 7.0, 150 mM NaCl, 300 mM imidazole and ligand). After elution, any remaining excess fluorophore was removed by exchanging the sample into a final buffer (25 mM HEPES pH 7.0, 75 mM NaCl, and ligand) using a PD-10 desalting column (Cytiva). All buffers were prepared with a saturating concentration of ligand or without ligand added (apo).

Radioligand binding assays for $A_{2A}AR$ in lipid nanodiscs

Radioligand binding assays were performed with the same samples of $A_{2A}AR$[A289C] used for single molecule fluorescence experiments; i.e., in nanodiscs containing the same lipid composition and with the Cy3 fluorophore covalently attached at position 289. For the displacement binding experiments, increasing concentrations of cold ligands were incubated with the radioligand [^{3}H]ZM241385 (American Radiolabeled Chemicals, St. Louis, MO) and with 0.125-0.25 μg of nanodiscs containing $A_{2A}AR$ in buffer containing 25 mM HEPES pH 7.0 and 75 mM NaCl for 60 min at room temperature. Binding reactions were terminated by filtration using the Microbeta filtermat-96 cell harvester (PerkinElmer, Waltham, MA) and radioactivity was measured using a MicroBeta2 microplate counter (PerkinElmer, Waltham, MA). Specific binding at $A_{2A}AR$ was determined as the difference in binding obtained in the absence and presence of 10 μM ZM241385.

Single-molecule fluorescence data acquisition

Single-molecule fluorescence data were recorded using a customized prism-based TIRF imaging system based on an inverted IX73 microscope (Olympus) and customized TIRF stage (TIRF Labs Inc., Cary, NC, U.S.A.) as described in earlier publications (Berezhna et al., 2012; Stefanski et al., 2021). Quartz microscope slides (G. Finkenbeiner, Waltham MA) and coverslips were cleaned and passivated with polyethylene glycol (m-PEG-SVA) and 3% biotin-PEG-SVA (Laysan Bio Inc, Arab, AL) as previously described (Lamichhane et al., 2010). A sample chamber was prepared using PEGylated slides and coverslips using double-sided tape and coated with 0.02 mg/mL streptavidin (Stefanski et al., 2021). Nanodiscs containing $A_{2A}AR$ and 5% biotin-PE in imaging buffer (20 mM HEPES pH 7.5, 75 mM NaCl, 2 mM Trolox and saturating concentration of ligand or no ligand added) were introduced into the sample chamber and incubated for 10 minutes. The sample chamber then was rinsed with imaging buffer to remove any nonspecific molecular species. The chamber was rinsed with glucose oxidase and a catalase oxygen scavenging system in imaging buffer and excited using a green (532 nM) laser. The emission intensities from the Cy3 fluorophore were collected on an EMCCD camera (Andor Technology) with 100 ms integration time using a custom single-molecule data acquisition program (Stefanski et al., 2021). Single-molecule time trajectories were extracted using scripts written in IDL software (Harris Geospatial Solutions, Inc). The package for data acquisition and extraction was downloaded from the laboratory of Dr. Taekjip Ha (http://ha.med.jhmi.edu/resources/).

Molecular dynamics simulations

Molecular dynamics (MD) simulations of $A_{2A}AR$ with the Cy3 fluorophore conjugated to cysteine 289 were performed using three different initial configurations of the receptor structure. The initial configuration of antagonist-bound $A_{2A}AR$ was modeled from the crystal structure of $A_{2A}AR$ in complex with the antagonist ZM241385 and with a coordinated sodium ion in a putative allosteric site (PDB ID 4EIY) (Liu et al., 2012). Agonist-bound $A_{2A}AR$ was modeled from the crystal structure of $A_{2A}AR$ in complex with NECA (PDB ID 2YDV) (Lebon et al., 2011). A tertiary complex of $A_{2A}AR$ was modeled from the crystal structure of $A_{2A}AR$ in complex with NECA and an engineered G protein (“mini $G\alpha_s$”; PDB ID 5G53) (Carpenter et al., 2016). The antagonist-bound $A_{2A}AR$ structure was prepared for MD simulations following previously reported procedures (Gutiérrez-de-Terán et al., 2013) that removed the non-native BRIL fusion protein used to facilitate crystallization and replaced the native residues in the third intracellular loops that were removed to facilitate crystallization. For agonist-bound $A_{2A}AR$, the point mutations introduced to increase the melting temperature of the receptor for crystallization were reverted to their native amino acid types with Pymol (Schrodinger, 2015). Protons were added to all structures, and the protonation states of titratable residues, including histidine, were calculated and the hydrogen bonding network optimized with the protein preparation wizard tool in Maestro (Sastry et al., 2013). For all three structures, the native

Ala289$^{7.54}$ sidechain was replaced with cysteine, and the Cy3 fluorophore was modeled with manual covalent docking using a 3D-optimized conformation of the fluorophore built in Maestro and further optimized with the Macromodel tools within the Schrödinger suite (Schrödinger, 2021).

Each receptor construct was inserted into a solvated membrane model and equilibrated following the PyMemDyn protocol (Esguerra et al., 2016; Gutiérrez-de-Terán et al., 2013). The starting structures are automatically embedded in a pre-equilibrated membrane consisting of POPC lipids, and the transmembrane bundle was aligned to its vertical axis, i.e., the bundle of helices was aligned parallel to the Z-axis. This hexagonal-prism shaped box is then soaked with bulk water and energy minimized with GROMACS 4.6 (Hess et al., 2008) using the OPLS-AA/M force field (Robertson et al., 2015) for the receptor and ligands and with Berger parameters for the lipids (Berger et al., 1997) together with the use of the half-e double-pairlist method (Chakrabarti et al., 2010) and the SPC water model (Berendsen et al., 1981). The same setup is used for a 2.5 ns MD equilibration under periodic boundary conditions (PBC), where initial restraints on receptor and ligand atoms are gradually released, followed by another 2.5 ns MD where only the distance restraints between interhelical contacts in class-A GPCRs were imposed, as previously described in detail (Esguerra et al., 2016). OPLS compatible parameters for all organic molecules (ZM241385, NECA and Cy3 maleimide) were generated with the LigParGen server (Dodda et al., 2017) and translated into GROMACS with ad hoc scripts. For the Cy3 maleimide covalently attached to Cys289$^{7.54}$ a pseudoresidue was manually created. Each system was then subject to three replica MD simulations in GROMACS, each lasting for 0.5 ms. The isobaric NPT ensemble was used with a Nose-Hoover thermostat (Hoover, 1985; Nosé, 1984) with a target temperature of 310 K. Electrostatic interactions beyond a cutoff of 12 Å were estimated with the particle mesh Ewald method, and a 2 fs time step was used combined with the LINCS algorithm (Hess et al., 1997). All MD analyses were conducted with the mdtraj library (McGibbon et al., 2015). Molecular superimpositions, trajectory visualizations, and molecular images were performed with PyMOL. Analysis of the trajectories was performed with the MDtraj package (McGibbon et al., 2015).

QUANTIFICATION AND STATISTICAL ANALYSIS

Single-molecule fluorescence data analysis

Single-molecule fluorescence time trajectories were assessed and analyzed using custom software written in Matlab. Individual trajectories were selected for further analysis from trajectories with single-step photobleaching that displayed reversible fluorescent intensity fluctuations at different intensity states before bleaching, which are described as dynamic traces. Individual dynamic traces were background corrected and normalized to the mean value of the lower-intensity state, which is defined as a value of “1”. Each trace was truncated before photobleaching, and the traces were binned and compiled to generate intensity histograms.

Histograms for each A_{2A}AR complex and for apo A_{2A}AR were generated by compiling more than 200 normalized single-molecule traces from at least two independent experiments. Error bars on histograms are the standard error calculated from at least 5 independent movies used to generate the histograms. Similar approaches were also used to report error bars previously (Liauw et al., 2021). To fit and process histograms, we used the Igor Pro software (version 8.04, Wavemetrics, Lake Oswego, OR, USA). In more detail, histograms for apo and antagonist-bound A_{2A}AR were fit with two Gaussian distributions, and agonist-bound A_{2A}AR three Gaussian distributions using Igor’s Multipeak Fit 2 function as shown in Equations 1 and 2, respectively.

$$y = y_0 + A_1 \exp\left\{-\left(\frac{x-b_1}{w_1}\right)^2\right\} + A_2 \exp\left\{-\left(\frac{x-b_2}{w_2}\right)^2\right\} \qquad \text{(Equation 1)}$$

$$y = y_0 + A_1 \exp\left\{-\left(\frac{x-b_1}{w_1}\right)^2\right\} + A_2 \exp\left\{-\left(\frac{x-b_2}{w_2}\right)^2\right\} + A_3 \exp\left\{-\left(\frac{x-b_3}{w_3}\right)^2\right\} \qquad \text{(Equation 2)}$$

In the equations above, y_0 is a baseline, A is the peak amplitude, b is the intensity peak center, and w is the peak width. The Find Peaks algorithm was used to locate the number of peaks and fit those peaks using the mean conformational states as peak centers calculated from the transition density plots. We used 1.0, 1.9, and 2.6 normalized intensity peak centers to fit the peaks from states 1, 2, and 3, respectively. The third peak was not populated for Apo and ZM bound samples, so those data were fit with two distributions. After fitting, the area of individual peaks was calculated from the A and w values obtained from the fit.

A Hidden Markov model was used to fit individual trajectories into different states with the HaMMy program (McKinney et al., 2006). Transition density plots were generated from the HaMMy fitted data that provided the transition events between different states. We used custom software written with Python to generate the transition density plots (Pauszek III et al., 2021).

Quantification and analysis of ligand binding for A_{2A}AR in lipid nanodiscs

IC_{50} values were determined using a nonlinear, least-squares regression analysis by Prism 8 (GraphPad Software). IC_{50} values obtained from the displacement curves were converted to K_i values using the Cheng-Prusoff equation (Cheng and Prusoff, 1973). Data are expressed as the mean ± the standard error from three independent experiments performed in triplicate.